Quantum critical dynamics for a prototype class of insulating antiferromagnets

Jianda Wu, Wang Yang, Congjun Wu, and Qimiao Si

Quantum critical dynamics for a prototype class of insulating antiferromagnets

Jianda Wu,[1] Wang Yang,[1] Congjun Wu,[1] and Qimiao Si[2]

[1]*Department of Physics, University of California, San Diego, California 92093, USA*
[2]*Department of Physics and Astronomy and Center for Quantum Materials, Rice University, Houston, Texas 77005, USA*

Quantum criticality is a fundamental organizing principle for studying strongly correlated systems. Nevertheless, understanding quantum critical dynamics at nonzero temperatures is a major challenge of condensed matter physics due to the intricate interplay between quantum and thermal fluctuations. The recent experiments in the quantum spin dimer material TlCuCl$_3$ provide an unprecedented opportunity to test the theories of quantum criticality. We investigate the nonzero temperature quantum critical spin dynamics by employing an effective $O(N)$ field theory. The on-shell mass and the damping rate of quantum critical spin excitations as functions of temperature are calculated based on the renormalized coupling strength, which are in excellent agreements with experiment observations. Their $T \ln T$ dependence is predicted to be dominant at very low temperatures, which is to be tested in future experiments. Our work provides confidence that quantum criticality as a theoretical framework, being considered in so many different contexts of condensed matter physics and beyond, is indeed grounded in materials and experiments accurately. It is also expected to motivate further experimental investigations on the applicability of the field theory to related quantum critical systems.

I. INTRODUCTION

Quantum and thermal fluctuations combine to determine the overall nonzero-temperature quantum dynamics as well as thermodyanmics of strongly correlated many-body systems. A quantum critical point occurs at zero temperature when matter goes from one quantum ground state to another upon tuning a non-thermal parameter[1,2]. An illustration of a generic phase diagram of quantum phase transition is presented in Fig. 1. Physical properties around quantum critical points are of extensive current interest. For instance, quantum criticality gives rise to unusual spin dynamics in heavy fermion metals[3–5] and one-dimensional quantum magnets[6,7], as well as the non-Fermi liquid behavior and unconventional superconductivity in a variety of strongly correlated electron systems[1,8–10]. The corresponding real-frequency dynamics is in general difficult to calculate, especially at nonzero temperatures ($T > 0$). Indeed, even for quantum systems in one spatial dimension, analytical understandings of such dynamical properties are still limited[7,11–14].

Recently, the neutron scattering experiments in the three-dimensional quantum magnetic dimer compound TlCuCl$_3$ have provided an ideal testbed of quantum critical theory at an unprecedented level[16–19]. TlCuCl$_3$ undergoes a continuous quantum phase transition from the quantum disordered phase to the Néel ordered one with increasing pressure. At ambient pressure, the ground state is a dimerized singlet paramagnet with the gapped low-energy triplon (triplet state) excitations. Upon increasing pressure, the triplon band bottom is lowered, and, at a critical pressure, these excitations become gapless leading to a quantum phase transition into the Néel ordered ground state. Correspondingly, the low-energy phase is capatured by a generic 3 (space) + 1 (time) dimensional relativisitic O(3) quantum ϕ^4 theory[20,21] [Ap-
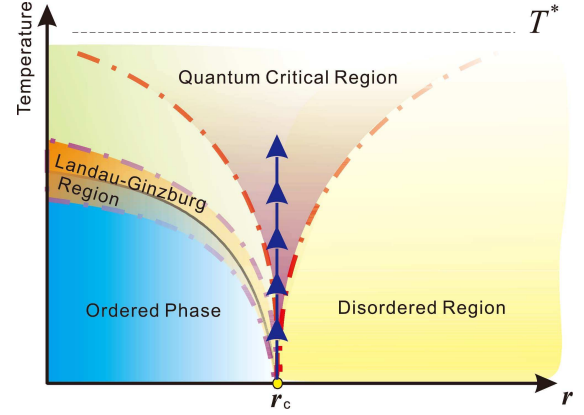

FIG. 1: Above figure depicts a generic phase diagram with a second order quantum phase transition, which arises in broad classes of systems[5,9,10,15,16]. The r and r_c denote tuning parameter and quantum critical point respectively. Due to different correlation characters resulting from the competition between thermal and quantum fluctuations, the whole diagram has been *de facto* divided into different regions as it is manifestly illustrated with different colors. The solid curve is used to denote a second order classical phase transition while the dot-dash curves illustrate crossover regions qualitatively. The broken line on the top is used to denote the cutoff temperature, T^*, beyond which quantum criticality is negligible. The dark blue arrow, flowing right upward from the QCP, shows the region we study in the main text.

pendix A]. While a great deal of efforts, such as theoretical proposals for detection of the Higgs mode and the ratio of gaps in disorder and order regimes, have been made towards understanding the experiments[22–27], the dynamics in the quantum critical regime have not been understood properly[28].

In this article, we study the critical dynamics of quantum antiferromagetism at nonzero temperatures by employing a generic 3 (space)+1 (time) dimensional relativistic $O(N)$-invariant quantum ϕ^4 theory. Both the on-shell and off-shell quantum critical dynamics at $T > 0$ are calculated in a broad dynamical regime. Our on-shell results for the mass and damping rate allow not only a qualitative understanding of the experimental observation but also a quantitative description of their magnitudes, and the $T \ln T$ dominance is found at very low temperatures. Moreover, the effective coupling of the field theory appropriate to systems such as TlCuCl$_3$ is determined, which will be important for further experimental means to test the applicability of the field theory to these materials. Studying the material and the quantum field theory serves as a means to explore the Higgs physics in a tabletop setting[29].

II. THE MODEL

We start with the following D-dimensional ($D = d + 1$) Euclidean relativistic Lagrangian with N-components $O(N)$ real field $(\phi_1, \phi_2, \cdots, \phi_N)$ [Appendix A],

$$\mathcal{L}_0 = \frac{1}{2}\Big(\partial_\nu \phi_i(\tau, \vec{x})\Big)^2 + \frac{g^2}{4!}\mu^{2\varepsilon}\phi_i^2(\tau, \vec{x})\phi_j^2(\tau, \vec{x}), \quad (1)$$

where the mass is set as zero at zero temperature corresponding to the quantum critical point, $\partial_\nu = (\partial_\tau, \partial_{\vec{x}})$, and μ is the energy scale parameter. In addition, g is the dimensionless coupling constant at the energy scale of μ. The ultraviolet (UV) divergent terms in the renormalization process will be absorbed by counter terms order by order in the framework of dimensional regularization (D-Reg), and ε is taken as zero for comparing theoretical results with experimental measurements. At the quantum critical point, the mass is renormalized to zero by definition. At nonzero temperatures, the mass only depends on temperature, therefore, the region we shall investigate is the one illustrated by the blue arrows in Fig. 1. The counter terms are not displayed but will be determined following the minimal-subtraction scheme[30].

We study $\mathcal{L}_0$ for the dynamics at nonzero temperatures within the Braaten-Pisarski resummation program, which is a systematic calculation machinery taking advantages of D-Reg and resummation[31-35]. The relevant diagrams up to 2-loop contributions are shown in Figs. S1 (a–h) in Appendix B. The finite-temperature renormalized theory at $N = 1$ was obtained previously in Refs.[36-40]. We consider the field theory with a general N, and the case of TlCuCl$_3$ corresponds to $N = 3$. Starting from $\mathcal{L}_0$, a 1-loop calculation for the self-energy or, the thermal mass, is based on the diagram of Fig. S1(a) in Appendix B, giving rise to

$$m_T^2 = -\Sigma_0(q) = a_N g^2(\mu)T^2 \quad (2)$$

with $a_N = (N + 2)/72$. By using the thermal mass, an effective field theory is constructed

$$\mathcal{L}_2 = \frac{1}{2}[(\partial_\mu \phi_i)^2 + m_T^2\phi_i^2] + \frac{1}{4!}g^2\mu^{2\varepsilon}\phi_i^2\phi_j^2 - m_T^2\phi_i^2/2 \quad (3)$$

with a new vertex $-\frac{1}{2}m_T^2\phi_i^2$ illustrated by Fig. S1(b)(Appendix B). $\mathcal{L}_2$ naturally cures the infrared (IR) divergence, equivalent to resumming the daisy diagrams (Fig. S2 in Appendix B based on $\mathcal{L}_0$[40]. This procedure leads to a non-analytic (in g^2) 1-loop renormalized mass,

$$m_T'^2 = m_T^2 - 3m_T^3/(\pi T) + O(g^4 \ln g), \quad (4)$$

showing the non-perturbative nature of the quantum ϕ^4 theory[37,40,41]. In order to determine the quantum dynamics, we proceed to the 2-loop level. Recognizing the 1-loop correction for the interaction (Fig. S1(c) Appendix B), a 1-loop zero-temperature interaction counter term (Fig. S1(d) in Appendix B) is incorporated to obtain the full 1-loop renormalized effective field theory $\mathcal{L}_3$,

$$\mathcal{L}_3 = \frac{1}{2}\left[(\partial_\mu \phi_i)^2 + m_T'^2\phi_i^2\right] + \frac{g^2}{4}\mu^{2\varepsilon}\phi_i^2\phi_j^2$$
$$- \frac{1}{2}m_T'^2\phi_i^2 + \frac{g^2\mu^{2\varepsilon}}{4!}\left[\frac{N+8}{6}\frac{g^2}{(4\pi)^2}\frac{1}{\varepsilon}\phi_i^2\phi_j^2\right] \quad (5)$$

which serves as the starting point for further calculations at the two-loop level.

From $\mathcal{L}_3$, via Figs. S1(a,b,e,f,g,h) (Appendix B), we obtain the renormalized self-energy to the order of g^4, $\Sigma_2 = \Sigma_2' + i\Sigma_2''$. The detailed expressions of Σ_2' and Σ_2'' are presented in Appendix C. For the long-wavelength physics, we fix the momenta for the external legs to be zero in the sunset diagram (Fig.S1(h) in Appendix B). The divergent terms associated with $\varepsilon \to 0$ are absorbed by counter terms for the wavefunction and momentum renormalizations, respectively. The detailed renormalzation calculation up to the two-loop level is given in Appendix C. The dynamical structure factor (DSF) is related to the self-energy through,

$$S(\omega, \vec{p} = 0) = \frac{2\mathrm{Im}[\chi(\omega, \vec{p} = 0)]}{1 - e^{-\beta\omega}}, \quad (6)$$

where $\chi^{-1}(\omega, \vec{p} = 0) = -\omega^2 + m_T'^2 - \Sigma_2(\omega)$, then the damping rate follows $\gamma = \Sigma_2''/(2\omega)$. In the following we will present the on-shell mass, and damping rates in three different frequency regimes. The comparison with the experiments on TlCuCl$_3$ will be discussed.

III. ON-SHELL DYNAMICS AND THE DAMPING RATE

A complex pole $\omega = M - i\gamma$ can be obtained from the zeros of $\chi^{-1}(\omega, \vec{p} = 0)$. Up to the two-loop level, the on-shell mass M is determined as

$$M^2(T) = a_N T^2 g^2(\mu)\{1 + b_N g^2(\mu)\ln(T/\mu)+$$
$$+ c_1 g(\mu) + c_2 g^2(\mu)\ln g^2(\mu) + c_3 g^2(\mu)\},(7)$$

where $b_N = (N + 8)/(48\pi^2)$, $c_1 = -3a_N^{\frac{1}{2}}/\pi$, $c_2 = 1/(8\pi^2)$, $c_3 = \{-(b_N/2)\ln(4\pi) + \ln a_N/(8\pi^2) + [\frac{3}{2}a_N\delta_0 + \delta_1/(16\pi^2)]\}$ with $\delta_0 = 5.242$, and $\delta_1 = 3.644$. In addition the $\ln T$ dependence in the big brackets arises from the sunset diagram (Eq. (C3) in Appendix C), signaling physics beyond scaling ansatz as will be discussed later. Around the complex pole, the renormalized propagator is well approximated by

$$\chi^{-1}(\omega, \vec{p} = 0) = -\omega^2 + M^2 - i\Sigma_2''(\omega). \quad (8)$$

Substituting the expression of Σ_2'' in Appendix C, the on-shell damping rate reads

$$\gamma(\omega^2 = M^2, \vec{p} = 0) = g^2 m_T/(64\pi). \quad (9)$$

In fact, the renormalized mass $M^2(T)$ in Eq. (7) is independent on the choice of the energy scale μ. To verify this at the two-loop level, we employ the μ-dependence of coupling strength $g(\mu)$ by solving the one-loop renormalization group equation[41-43],

$$g^2(\mu) = \frac{g^2(\mu_0)}{1 + b_N g^2(\mu_0)\ln(\mu_0/\mu)}. \quad (10)$$

μ_0 is a reference energy scale, which for convenience is set at $\mu_0 = T$ throughout the rest part of the paper[44]. From Eq. (10), to the order of g^4, we arrive at

$$g^2(\mu_0 = T) = g^2(\mu)[1 + b_N g^2(\mu)\ln(T/\mu)] + O(g^6(\mu)), \quad (11)$$

which apparently pushes the μ-dependence of the two-loop mass Eq. (7) to the next order $g^5 \ln g$.

While our theoretical renormalization procedure is general, the strategy for comparison with the experimental data is as follows. We start with a particular temperature $T = T_1$, set as μ_0. The value of $g(\mu_0 = T_1)$ is fitted by comparing the thermal mass Eq. (7) in which μ is set as μ_0 with the experimental data at $T = T_1$. For data measured at a different temperature, say, T_2, Eq.(10) is used to determine $g(\mu = T_2)$, based on which, the mass and damping rates at T_2 are calculated and compared with the experimental data. As will be clear later, excellent agreements with experiemnial results are achieved for independent data points of masses and damping rates.

In principle, the temperature for any data point can be served as a renormalization reference point. For later convenience, we choose maximal temperature, $T = T_{\exp}^{\max} \approx 12K$, at which the data was measured. Correspondingly, based on Eq. (7), the initiative $g(\mu_0 = T_{\exp}^{\max}) \approx 4.15$ by substituting $N = 3$, and Fig. 2 illustrates the flow of $g(\mu)$ at different energy scales. The advantage of this choice is that the coupling constant $g(\mu)$ determined at lower energy scales becomes smaller, which improves the accuracy of the perturbative calculation. In particular, the validity of the perturbation theory can only be justified at μ far less than the scale of Landau pole. Our calculation shows that the Landau pole based on Eq. (10) is located at the energy scale about
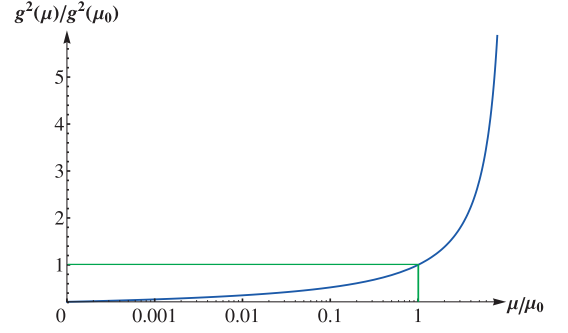

FIG. 2: Coupling strength at different physical energy scale, μ, following Eq. (10). Here, the reference coupling $g(T) = 4.146$, and the Landau pole occurs at $\mu_L = 12.253T$.
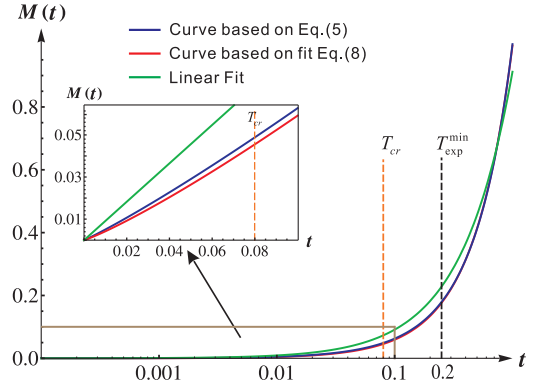

FIG. 3: Two-loop renormalized mass $v.s.$ reduced temperature t. The blue curve is based on Eq. (7). It is approximated by Eq. (12) and $M(T) = 0.91t$ illustrated by red and green curves, respectively. The black and orange broken lines respectively mark the minimal experimental temperature, and the crossover temperature when the $T \ln T$ behavior starts to become dominant. The inset figure zooms in the low temperature region ($t < 0.1$), which clearly shows that the mass behavior significantly deviates from the linear-T behavior.

$\mu_L = 12.25T_{\exp}^{\max}$, which is well beyond the temperature scope measured.

Following this procedure, we plug the obtained coupling constant at each temperature into Eq. (7) to obtain the two-loop renormalized mass as plotted in Fig. 3. For later convenience, the calculated masses can be approximated by (the mass here is reduced by $T_{\exp}^{\max}$)

$$M(T) = 1.00t/[1.00 + 0.30\ln(1/t)] \quad (12)$$

with $t = T/T_{\exp}^{\max}$. The linear-T behavior dominates at relatively high temperature in which the experiment measurements were performed. As lowering the temperature, the $T \ln T$ correction becomes important and dominates in the very low temperature region. This expression can be understood as follows: By setting $\mu = T$ in Eq. (7), the leading contribution to $M(T) \sim Tg(\mu = T)$. The deviation from the linear-T behavior of $M(T)$ is due to
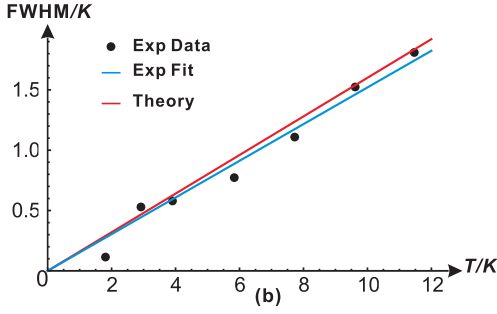
FIG. 4: Temperature dependence of the damping rate. Here, our theoretical result FWHM $= 0.16T$ (red line) is shown along with the experimental result of Ref.[16], which includes the values (without error bars) at different temperatures (black dots) and a fit of these values in terms of FWHM $= 0.15T$ (blue line).

FIG. 5: A schematic plot of the dynamical structure factor at zero momentum, describing the behavior in different asymptotic regimes: on-shell ($\omega \sim M$) and off-shell at $\omega \ll M$ and $\omega \gg M$. The dash lines interpolate among these regimes.

the weakening of $g(\mu = T)$ as lowering T according to the running coupling constant expression Eq. (10). The corresponding crossover temperature scale can be determined as

$$T_{cr} \sim \mu_0 e^{-1/[b_N g^2(\mu_0)]} \qquad (13)$$

with $\mu_0 = T_{\exp}^{\max}$. In our case, $T_{cr} \approx 1\text{K}$ corresponding to $t \approx 0.08$, which is about half-order smaller than the lowest temperature in experiments. Therefore in the range of experiment measurement temperatures Eq. (12) gives a theoretical prediction of mass $M_{\text{th}} \approx 1.00T$ which excellently agrees with the experimental result $M_{\exp} = T$ 16. However, for the material of TlCuCl$_3$, there exists a small gap induced by anisotropy $\Delta \approx 0.38\text{meV}$[19], which spoils the $O(3)$ invariance. Since this temperature scale (Δ) is much larger than T_{cr}, we are not optimistic at the experimental observation of the $T \ln T$ behavior in the material of TlCuCl$_3$. However, we expect that the $T \ln T$ behavior should be observed for the material which can be effectively described by the $\mathcal{L}_0$ [Eq. (1)] at low enough temperatures.

We proceed to analyze the damping rates in the experimental relevant region, namely, the linear-T-dominant region in Fig. 3. After some calculations, we arrive at $\gamma_{\text{th}}(\mu = T) \approx 0.08T$ for $N = 3$. Correspondingly, the full width at half maximum (FWHM) scales as FWHM$_{\text{th}} \approx 0.16T$ which excellently agrees with the experimental observation of FWHM$_{\exp} \approx 0.15T$[16] (Fig. 4). Our calculation is exact at two-loop, g^4. However, from Eq. (9), it is observed that the mass at the one-loop level (g^2) has already resulted in the damping rate at the order of g^4 (two loops). Nevertheless, the mass will exhibit the logarithmic dependence at low temperatures, therefore, we still expect the linear-T behavior for the on-shell damping rate will also be spoiled when temperature is decreased further to the $T \ln T$ dominant region, which should be verified when the field-theory approach is pushed to the order of g^6 (three loops).

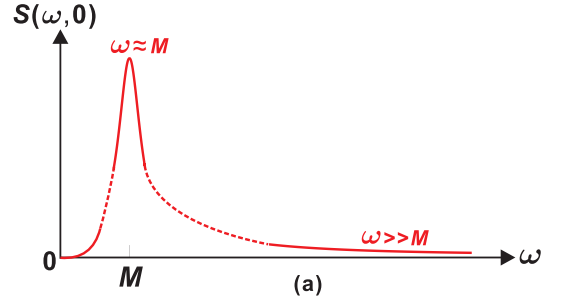The striking agreement between our theoretical results

and the experiment indicates that the $3 + 1$ dimensional $O(3)$ relativistic quantum field theory takes an excellent account of the underlying physics near the pressure-induced quantum critical point of TlCuCl$_3$. Furthermore, for the initiative g, we have $g^2/4! \approx 0.7$. This value implies that the interaction among the critical modes is significant but still moderate, allowing for a loop expansion to extract semi-quantitative results for the pertinent physical properties. Furthermore, one must proceed to at least two loop (g^4) to obtain a physical prediction of the $T \ln T$ dominance. Following our two-loop renormalization analysis we expect a clear $T \ln T$-dominant behavior for the mass at low temperatures, which goes well beyond conventional scaling ansatz.

IV. OFF-SHELL DYNAMICS AT FREQUENCIES FAR AWAY FROM M

We first determine the damping rate in the zero frequency limit, $\omega \ll M$. The imaginary part of the self-energy $\Sigma_2''(q = 0, \omega)$ can be organized into the imaginary part of G_0, G_1 and G_2 as shown in Eqs. (S6-S9) in Appendix C, which arise from the contribution of of the sunset diagram (Fig. S1(h) in Appendix B). In the low frequency limit, due to the on-shell energy-momentum conservations, there is no contribution from G_0 because of a three-particle threshold. The phase space that satisfies the on-shell constraints lies in the large momentum regime. Because of the Bose-distribution factor, the contributions from G_1 and G_2 are exponentially suppressed. Our calculation shows that

$$\begin{aligned} \gamma \;\sim\; & T^2 \exp[-(m_T/T)(m_T/\omega)]/(2\omega) \\ \sim\; & T \exp[-g^2 T/\omega)]/(2(\omega/T)) \to 0 \;\; (\omega \to 0). \;\; (14) \end{aligned}$$

This exponentially small result is subleading compared to the perturbative renormalized theory we carried out at the order of g^4. As a consequence of the suppressed spectral weight in this regime, the analysis is beyond the scope of the procedure outlined here.

We next consider the damping rate in the large frequency limit, $\omega \gg M$, for which the physical energy scale should be set by $\mu = \omega$. On the other hand, the perturbative framework stops working at the energy scale of the Landau pole $\mu_L = \exp\left\{1/[b_N g(T)^2]\right\}$ determined by Eq. (10). Thus, we work in the range $M(\mu = \omega) \ll \omega \ll \mu_L$. In the large frequency limit, the dominant contribution to Σ_2'' comes from $\mathrm{Im}G_0$. Evaluating the integration for $\mathrm{Im}G_0$ exactly yields $\mathrm{Im}G_0(\omega^2, \vec{p} = 0) \sim g^4(\omega)\omega^2$ (Appendix C), correspondingly, $\gamma \sim g^4(\omega)\omega$ and $S(\omega, \vec{p} = 0) \sim \omega^{-2}$. In this regime, the system is over-damped. A logarithmic correction naturally arises from $g^2(\omega)$ determined from Eq. (10), but is of the order g^6. The overall behavior of the DSF is shown in Fig. 5, which we expect to be experimentally observed in the near future in proper strongly correlated systems.

V. DISCUSSIONS

We note that any physical observable should be cut-off independent. Our results satisfy this requirement at the two-loop level, while, in contrast, previous results along these lines are cut-off independent only at the order of one loop[28]. Improvement is significant and fundamental rather than technical, since it brings qualitatively new behavior of the mass as well as the dynamic information: The $T \ln T$ behavior beyond the scaling ansatz emerges only at the two-loop level; it cannot be accessed by the method of [28], being correct at one loop only and accurate up to the order of g^3 (or $\alpha^{3/2}$ in the notations of that study); accordingly, the two-loop RG invariant mass as presented in Eq. (7) here does not obtain by the method of [28]. There are also differences between our study and that of [28] so far as the potential for guiding experiments is concerned, and we believe that, also here, there are considerable advantages in using our approach.

We now remark on a few points. First, the two-loop calculation has incorporated all the pertinent terms at the order of g^4. There are an infinite number of other diagrams which can contribute to the order of g^4; for example, if adding one more bubble in Figs. S1(e,f,h) (Appendix B) or one more blob (two-point interaction vertex) in the Fig. S1(h), their contribution is at the order of g^4. However, when summing over all of these kinds of diagrams, their contributions at the order of g^4 exactly cancel with each other[37], leaving a final contribution at the three-loop level. The procedure can in principal be carried out order by order, leading to any desired accuracy for the (on-shell) quantum critical dynamics at nonzero temperatures of the relativistic 3+1 dimensional $O(N)$ quantum ϕ^4 theory[35]. In our study, the result at the two-loop level is already in an excellent agreement with the experiments. We have also demonstrated that the effective coupling constant provides a justification for the two-loop calculation.

Second, our analysis is asymptotically exact for $D = 3 + 1$ dimensions, where all the UV divergences are systematically absorbed by counter terms controlled by the small quantity ε. These UV divergences associated with ε yield proper wave-function and momentum renormalizations order by order in the form of counter terms[37], which in turn modify the next-leading-order behavior. In other words, ε can only be taken to zero when, at each order, the contributions from the previous-order counter-terms have been incorporated. For lower-dimensional systems, say, in two spatial dimensions, the corresponding problem can be analyzed by setting $\varepsilon = 1/2$. We want to emphasize the difficulty in removing the IR singularities. Not in every field theory can one remove its IR singularities[40]. It is fortunate that there is a systematic way to regularize the $3 + 1$ dimensional quantum ϕ^4-theory However, the resummation in the calculation paradigm is essentially non-perturbative, which gives rise to non-analytical corrections beyond the perturbation series, therefore, the procedure can become very involved when one tried to push to higher orders.

Third, the leading behavior we obtained for TlCuCl$_3$ is expected, from the perturbation view point, to hold when $|m^2(T = 0)| \ll T$ (Fig. 1, also called as high-T regime[2]). However, when one moves to the regime $|m^2(T = 0)| \gg T$ (also called as low-T regime[2]) the non-critical background does become important. For obtaining a correct understanding one not only needs to introduce new counter terms associated with the open gap to cure newly appeared UV divergences, but also require new techniques beyond the current approach to access the physics in the ordered regime especially near the transition line[45]. These new must-introduced techniques and the expected new physics compose a new challenging goal worthy of further exploration.

VI. CONCLUSIONS

We have studied the quantum critical dynamics at nonzero temperatures based on a generic 3+1 dimensional relativistic quantum ϕ^4 theory and compared the results with the spin dynamics experiments on the insulating antiferromagnet TlCuCl$_3$. The theoretical coupling constant is determined from the temperature dependence of the thermal mass corresponding to the gap value. The resulting mass and damping rate are consistent with the experimental data. The logarithmic behavior is predicted to be dominant at extremely low temperature which should be observable in a proper experimental setup. At last, the damping behavior over a broad dynamical regime is also determined for comparison with future experiments. In turn, our results provide concrete evidence for the applicability of the underlying quantum field theory to the description of the observed quantum critical point. This, together with the quantitative determination of the effective coupling constant, will allow for the calculation of additional experimental observable such as the nuclear magnetic resonance (NMR) relaxation rate. From a theoretical perspective, knowledge on

the dynamical properties of generic quantum field theory deepens our understandings on not only condensed matter systems but also the dynamical processes in high-energy and cosmology physics[46]. Our calculation represents progress in a theory that is grounded in a concrete and prototype condensed matter system.

VII. ACKNOWLEDGEMENTS

[1] Special issue on Quantum Phase Transitions, J. Low Temp. Phys. **161**, 1 (2010).

[2] S. Sachdev, *Quantum PhaseTransitions* (Cambridge University Press, Cambridge, 2011), 2nd ed.

[3] Q. Si, S. Rabello, K. Ingersent, and J. L. Smith, Nature **413**, 804 (2001).

[4] A. Schröder, G. Aeppli, R. Coldea, M. Adams, O. Stockert, H. Löhneysen, E. Bucher, R. Ramazashvili, and P. Coleman, Nature **407**, 351 (2000).

[5] E. Schuberth, M. Tippmann, L. Steinke, S. Lausberg, A. Steppke, M. Brando, C. Krellner, C. Geibel, R. Yu, Q. Si, et al., Science **351**, 485 (2016).

[6] A. W. Kinross, M. Fu, T. J. Munsie, H. A. Dabkowska, G. M. Luke, S. Sachdev, and T. Imai, Phys. Rev. X **4**, 031008 (2014).

[7] J. Wu, M. Kormos, and Q. Si, Phys. Rev. Lett. **113**, 247201 (2014).

[8] P. Coleman and A. J. Schofield, Nature **433**, 226 (2005).

[9] Q. Si and F. Steglich, Science **329**, 1161 (2010).

[10] J. Wu, Q. Si, and E. Abrahams, Phys. Rev. B **93**, 104515 (2016).

[11] P. Deift and X. Zhou, NATO Adv. Sci. Ins. Ser., Ser. B **320**, 183 (1994).

[12] S. Sachdev and A. P. Young, Phys. Rev. Lett. **78**, 2220 (1997).

[13] J. S. Caux and R. Hagemans, J. Stat. Mech. Theor. and Exp. **2006**, P12013 (2006).

[14] J. S. Caux, H. Konno, M. Sorrell, and R. Weston, Phys. Rev. Lett. **106**, 217203 (2011).

[15] A. Millis, Phys. Rev. B **48**, 7183 (1993).

[16] P. Merchant, B. Normand, K. Krämer, M. Boehm, D. Mc-Morrow, and C. Rüegg, Nat. Phys. **10**, 373 (2014).

[17] C. Rüegg, A. Furrer, D. Sheptyakov, T. Strässle, K. W. Krämer, H.-U. Güdel, and L. Mélési, Phys. Rev. Lett. **93**, 257201 (2004).

[18] C. Rüegg, B. Normand, M. Matsumoto, C. Niedermayer, A. Furrer, K. W. Krämer, H.-U. Güdel, P. Bourges, Y. Sidis, and H. Mutka, Phys. Rev. Lett. **95**, 267201 (2005).

[19] C. Rüegg, B. Normand, M. Matsumoto, A. Furrer, D. F. McMorrow, K. W. Krämer, H. U. Güdel, S. N. Gvasaliya, H. Mutka, and M. Boehm, Phys. Rev. Lett. **100**, 205701 (2008).

[20] S. Chakravarty, B. I. Halperin, and D. R. Nelson, Phys. Rev. B **39**, 2344 (1989).

[21] A. V. Chubukov, S. Sachdev, and J. Ye, Phys. Rev. B **49**, 11919 (1994).

[22] Y. Kulik and O. P. Sushkov, Phys. Rev. B **84**, 134418 (2011).

[23] S. Jin and A. W. Sandvik, Phys. Rev. B **85**, 020409 (2012).

[24] K. Chen, L. Liu, Y. Deng, L. Pollet, and N. Prokof'ev, Phys. Rev. Lett. **110**, 170403 (2013).

[25] H. D. Scammell and O. P. Sushkov, Phys. Rev. B **92**, 220401 (2015).

[26] W. Witczak-Krempa, Phys. Rev. Lett. **114**, 177201 (2015).

[27] Y. Q. Qin, B. Normand, A. W. Sandvik, and Z. Y. Meng, arXiv:1506.06073 (2015).

[28] H. Scammell and O. Sushkov, Phys. Rev. B **95**, 024420 (2017).

[29] http://www.nature.com/news/higgs-physics-on-the-cheap-1.12682.

[30] B. de Wit and J. Smith, *Field Theory in Particle Physics* (North-Holland, Amsterdam, 1986).

[31] R. D. Pisarski, Nucl. Phys. B **309**, 476 (1988), ISSN 0550-3213.

[32] R. D. Pisarski, Phys. Rev. Lett. **63**, 1129 (1989).

[33] E. Braaten and R. D. Pisarski, Nucl. Phys. B **337**, 569 (1990).

[34] R. D. Pisarski, Nucl. Phys. A **525**, 175 (1991).

[35] J. O. Andersen and M. Strickland, Ann. Phys. **317**, 281 (2005).

[36] N. Banerjee and S. Mallik, Phys. Rev. D **43**, 3368 (1991).

[37] R. R. Parwani, Phys. Rev. D **45**, 4695 (1992).

[38] R. R. Parwani and H. Singh, Phys. Rev. D **51**, 4518 (1995).

[39] E. Wang and U. Heinz, Phys. Rev. D **53**, 899 (1996).

[40] M. Laine, *Basics of thermal field theory* (Lecture notes from University of Bielefeld, Germany, 2015).

[41] M. D. Schwartz, *Quantum Field Theory and the Standard Model* (Cambridge University Press, 2013).

[42] J. Frenkel, A. V. Saa, and J. C. Taylor, Phys. Rev. D **46**, 3670 (1992).

[43] P. Arnold and C. Zhai, Phys. Rev. D **50**, 7603 (1994).

[44] In the continuum renormalization group, we use only renormalized quantities. The UV divergences are taken care of by the poles in ϵ, while the IR divergences are treated via re-summation. The μ here plays the role of a physical energy scale[41].

[45] M. Pietroni, Phys. Rev. Lett. **81**, 2424 (1998).

[46] A. V. Bednyakov, B. A. Kniehl, A. F. Pikelner, and O. L. Veretin, Phys. Rev. Lett. **115**, 201802 (2015).

[47] N. Cavadini, W. Henggeler, A. Furrer, H.-U. Güdel, K. Krämer, and H. Mutka, Euro. Phys. J. B - Cond. Mat.

and Comp. Sys. **7**, 519 (1999).

[48] N. Cavadini, G. Heigold, W. Henggeler, A. Furrer, H. Güdel, K. Krämer, and H. Mutka, J. Phys.: Cond. Mat. **12**, 5463 (2000).

[49] N. Cavadini, G. Heigold, W. Henggeler, A. Furrer, H.-U. Güdel, K. Krämer, and H. Mutka, Phys. Rev. B **63**, 172414 (2001).

[50] A. Oosawa, T. Kato, H. Tanaka, K. Kakurai, M. Müller, and H.-J. Mikeska, Phys. Rev. B **65**, 094426 (2002).

[51] S. Sachdev and R. Bhatt, Phys. Rev. B **41**, 9323 (1990).

[52] D. C. Cabra, A. Honecker, and P. Pujol, *Modern theories of many-particle systems in condensed matter physics*, vol. 843 (Springer Science & Business Media, 2012).

Appendix A: A Brief Derivation for Eq. (1) in Main Text

Each unit cell of TlCuCl$_3$ consists of a dimer formed by two magnetic spin-$\frac{1}{2}$ Cu^{2+} ions, and the centers of the dimers form a three-dimensional cubic lattice. The intra- and inter-dimer antiferromagnetic exchange interactions are modeled as

$$H = J \sum_{\mathbf{r}} \mathbf{S}_{\mathbf{r},1} \cdot \mathbf{S}_{\mathbf{r},2} + \lambda J \sum_{\langle \mathbf{r},\mathbf{r}' \rangle;\ l=1,2} \mathbf{S}_{\mathbf{r},l} \cdot \mathbf{S}_{\mathbf{r}',l} ,\quad \text{(A1)}$$

where $\mathbf{r}$ represents the central position of the dimer, and l is the site index inside the dimer; $\mathbf{S}_{\mathbf{r},1}$ are spin-$\frac{1}{2}$ operators; $\langle \cdots \rangle$ denotes summation over the nearest neighbours. In addition, J (> 0) and λJ ($0 \leq \lambda \leq 1$) denote the intra- and inter- dimer coupling strengths respectively. The next-next-nearest neighbour interactions[47–50] are sub-leading and neglected. When $\lambda = 0$ the ground state is a paramagnetic state with separable singlet states; when $\lambda = 1$, H describes the cubic lattice antiferromagnet with a long range Néel order. Therefore, a quantum phase transition arises when λ is tuned to a critical value λ_c. The observed strong intra-dimer interaction[47–50] indicates the dominant low-lying excitations are spin triplets, therefore, it is proper to introduce bond-operators $s^\dagger(\mathbf{r})$ and $t_\alpha^\dagger(\mathbf{r})(\alpha = x,y,z)$ for the dimer spin singlet and triplet states. They satisfy $s^\dagger(\mathbf{r})|0\rangle = \frac{1}{\sqrt{2}} [|\uparrow\downarrow\rangle_{\mathbf{r}} - |\downarrow\uparrow\rangle_{\mathbf{r}}]$, $t_+^\dagger(\mathbf{r})|0\rangle = -|\uparrow\uparrow\rangle_{\mathbf{r}}$, $t_z^\dagger(\mathbf{r})|0\rangle = \frac{1}{\sqrt{2}} [|\uparrow\downarrow\rangle_{\mathbf{r}} + |\downarrow\uparrow\rangle_{\mathbf{r}}]$, and $t_-^\dagger(\mathbf{r})|0\rangle = |\downarrow\downarrow\rangle_{\mathbf{r}}$ with $|0\rangle$ being a reference vacuum state with $t_\pm^\dagger = t_x \pm i t_y$[51]. In the continuum limit we express the t_α-field with $t_\alpha(\mathbf{r}) \sim a^{d/2} [\phi_\alpha(\mathbf{r}) + i\pi_\alpha(\mathbf{r})]$ ($\alpha = x,y,z$) where d is the spatial dimension and a is the lattice constant. π_α are conjugate momentum to ϕ_α satisfying $[\phi_\alpha(\mathbf{r}), \pi_\beta(\mathbf{r}')] = i\delta(\mathbf{r} - \mathbf{r}')\delta_{\alpha\beta}$. Taking advantage of the condensation of the s-field, we integrate over the π-field, leaving a Lagrangian density in the imaginary-time formalism as a functional of the ϕ-field up to quartic order[52],

$$\mathcal{L} = \chi(\partial_\tau \phi_\alpha)^2 + \rho_s(\nabla \phi_\alpha)^2 + m^2 \phi_\alpha^2 + u\phi_\alpha^2 \phi_\beta^2, \quad \text{(A2)}$$

where the parameters are estimated as $\chi \approx 1/J$, $\rho_s \approx 2za^2\lambda J$, $m^2 \approx J(1 - 4z\lambda)$ and $u \approx 2za^d\lambda J$ with z being
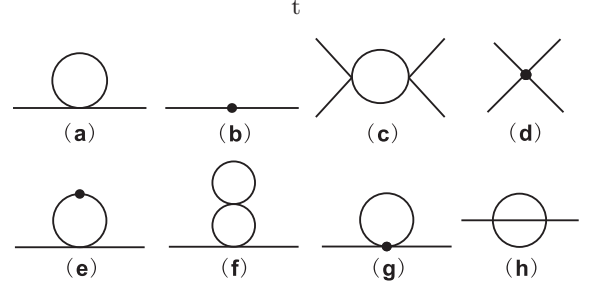

FIG. S1: (a) One-loop self energy diagram. (b) Two point effective interaction in $\mathcal{L}_2$. (c) One-loop correction to the four-point vertex. There are two additional crossed channels, which are not shown. (d) UV vertex counter term for the interaction. (e) Insertion of the finite two-point interaction in $\mathcal{L}_2$ into the one-loop self-energy (bubble) diagram. (f) Two-loop bubble diagram. (g) Self energy contribution from the UV vertex counter term. (h) Sunset diagram.
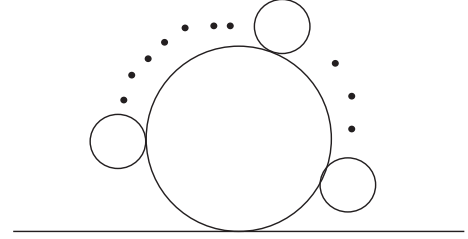

FIG. S2: A typical daisy diagram with m dressing bubbles for the $\mathcal{L}_0$ (Eq. (2) in main text).

the coordinate number, then the velocity of the field $c_0^2 = \rho_s/\chi \approx 2z\lambda a^2 J^2$. After normalizing $\mathcal{L}$ by ρ_s, setting $c_0^2 = 1$, $m^2 = 0$ and generalizing the field to N-components $O(N)$ field ($\phi_1, \phi_2, \cdots, \phi_N$), we recover the Lagrangian $\mathcal{L}_0$ Eq. (1) presented in the main text.

Appendix B: Relevant Feynman Diagrams up to Two Loops and A Typical Daisy Diagram for $\mathcal{L}_0$ and Resummation

Figs. S1(a–h) list relevant Feynman diagrams up to two loops.

A typical (one-loop) daisy diagram with m dressing bubbles for the $\mathcal{L}_0$ (Eq. (2) in the main text) is illustrated in Fig. (S2). The "resummation" of a series of this kind of diagrams helps remove the IR divergence for the $\mathcal{L}_0$. Higher order resummation diagrams can be similarly generated when we proceed to multi-loop situations. After adding proper UV counter terms and resummation of all daisy diagrams at each order the Lagrangian can then be updated to the next leading order. In this way it provides a systematic way to renormalize the $3 + 1$ dimensional quantum ϕ^4 theory.

Appendix C: Real and Imaginary Parts of Self Energy to Two Loops

Up to two loops, the renormalized real part of the self-energy gives,

$$\Sigma_2'(\omega^2) = \Sigma_{ren} + F_1 + F_2 + H \qquad \text{(C1)}$$

with

$$\Sigma_{ren} = \frac{3m_T^3}{\pi T} + \frac{3m_T^2}{4\pi^2}\left(\frac{m_T}{T}\right)^2 \ln\frac{4\pi\mu^2}{T^2} + \frac{3m_T^2}{2\pi^2}\left(\frac{m_T}{T}\right)^2\left(2c_1 - \frac{5}{2} - \frac{\gamma_E}{2}\right) \qquad \text{(C2)}$$

$$F_1 = \frac{N+2}{3}\frac{1}{(4\pi)^2}\frac{g^4 T^2}{24}\left(\ln\frac{4\pi\mu^2}{m_T'^2} + 2 - \gamma_E\right) \qquad \text{(C3)}$$

$$F_2 = \frac{N+2}{3}\frac{g^4}{8(2\pi)^4}\int_0^\infty \frac{kn_k dk}{E_k}\int_0^\infty \frac{dq}{E_q}\left(q\ln\left|\frac{X_+}{X_-}\right| - 4k\right) \qquad \text{(C4)}$$

$$H = \frac{N+2}{3}\frac{g^4}{8(2\pi)^4}\int_0^\infty \frac{kn_k dk}{E_k}\int_0^\infty \frac{qn_q dq}{E_q}\ln\left|\frac{Y_+}{Y_-}\right| \qquad \text{(C5)}$$

where $m_T'^2 = m_T^2 - 3m_T^3/(\pi T) + O(g^4\ln g)$ and Σ_{ren} comes from the renormalized contribution of Figs. S1(a,b,e,f,g). In addition $F_1, F_2(\omega^2)$ and $H(\omega^2)$ denote those from the real part of the sunset diagram Fig. S1(h), in which $c_1 = (2\gamma_E - 2\ln(4\pi) - 1)/4$, $X_\pm = [\omega^2 - (E_k + E_q + E_{k\pm q})^2][\omega^2 - (E_q - E_k + E_{k\pm q})^2]$, and $Y_\pm = X_\pm[\omega^2 - (E_k - E_q + E_{k\pm q})^2][\omega^2 - (E_k + E_q - E_{k\pm q})^2]$

with $E_l^2 = l^2 + m_T^2$, $n_l = 1/(e^{\beta E_l} - 1)$, $l = k, q$. (Here, γ_E is the Euler constant.)

The imaginary part of the self energy gives,

$$\Sigma_2''(\omega^2) = \text{Im}(G_0) + \text{Im}(G_1) + \text{Im}(G_2), \qquad \text{(C6)}$$

where

$$G_0 = g^4\int d[k,q]S(E_k, E_q, E_r) \qquad \text{(C7)}$$

$$G_1 = 3g^4\int d[k,q]n_k\left[S(E_k, E_q, E_r) + S(-E_k, E_q, E_r)\right] \qquad \text{(C8)}$$

$$G_2 = 3g^4\int d[k,q]n_k n_q[S(E_k, E_q, E_r) + S(-E_k, E_q, E_r) + S(E_k, -E_q, E_r) - S(E_k, E_q, -E_r)]. \qquad \text{(C9)}$$

Here, $S(E_k, E_q, E_r) = 1/(i\omega_n + E_k + E_q + E_r) + 1/(-i\omega_n + E_k + E_q + E_r)$, $E_k E_q E_r d[k,q] = [(N+2)/24](\mu^{4\varepsilon}/3!)[d^{D-1}k/(2\pi)^{D-1}][d^{D-1}q/(2\pi)^{D-1}]$, and $r = |\vec{k} + \vec{q}|$. When $N = 1$, our results are compatible to those of the scalar case[37].

(Eq. (C7)). Because of the on-shell energy-momentum conservations, the ε can be simply set to 0 for calculating the imaginary part of the self energy with the mass term replaced by a physical one. Evaluating the integration for $\text{Im}(G_0)$ yields

Appendix D: Imaginary Part of G_0 in the Large Frequency Limit

In the large frequency limit $(M(\mu = \omega) \ll \omega \ll \mu_L)$, the dominant contribution to Σ_2'' comes from $\text{Im}(G_0)$

$$\text{Im}G_0(\omega^2, \vec{p} = 0) \tag{D1}$$

$$= Ag(\omega)^4 \pi M^2 \left[\int_0^{y_1} \frac{y}{E_y} \left(\sqrt{f_4^2(y) + 1} - \sqrt{f_2^2(y) + 1} \right) dy + \int_{y_1}^{y_2} \frac{y}{E_y} \left(\sqrt{f_4^2(y) + 1} - \sqrt{f_3^2(y) + 1} \right) dy \right]$$

where $A = (N + 2)/(1152\pi^4)$, $x = k/M$, $y = q/M$, $y_1 = \sqrt{(z_0 - 1)(z_0 - 3)}/2$, $y_2 = \sqrt{(z_0^2 - 9)(z_0^2 - 1)}/(2z_0)$ with $z_0 = \omega/M$. In addition $x = f_3(y), f_4(y)$ are two solutions of $z_0 = \sqrt{x^2 + 1} + \sqrt{y^2 + 1} + \sqrt{(x - y)^2 + 1}$ with $f_2(y) =$ $-f_3(y)$ and $f_3(y) < f_4(y)$. In the large frequency limit we consider, $z_0 \gg 1$, $y_1 \approx z_0/2$ and $y_2 \approx y_1$, then the second integral is negligible. In addition, using $y_1 = z_0/2 \ll z_0$, we find $\text{Im}G_0(\omega^2, \vec{p} = 0) \sim g(\omega)^4 \omega^2$.